RSC Advances

PAPER

View Article Online
View Journal | View Issue

Cite this: *RSC Adv.*, 2025, **15**, 26013

Efficient Ag/La-ZnO core–shell catalyst for green synthesis of 4*H*-pyrano[2,3-*c*] pyrazoles†

Hrishikesh Labhade, *[ab] Sharad Gaikwad, [a] Jaidip Wable, [b] Amol Kategaonkar [a] and Samin Shaikh [c]

Received 21st April 2025
Accepted 14th July 2025

DOI: 10.1039/d5ra02788h

rsc.li/rsc-advances

The advancement of green and efficient synthetic strategies is essential for the pursuit of environmentally sustainable organic transformations. Pyrazole derivatives, recognized for their broad pharmacological and synthetic utility, are key structural motifs in various bioactive molecules. This study reports a one-pot, four-component (aryl aldehyde, malononitrile, ethyl acetoacetate, and hydrazine hydrate) synthesis of pyrazole derivatives catalyzed by lanthanum-doped and silver-coated ZnO (Ag/La-ZnO) core–shell nanoparticles under solvent-free grinding conditions at ambient room temperature. The catalyst was synthesized *via* a chemical precipitation method and comprehensively characterized using XRD, FTIR, BET, EDAX, FESEM, HRTEM, SAED, and XPS techniques. The synthesized pyrazoles were characterized using FTIR, ^{1}HNMR, ^{13}CNMR, and MS. Compared to conventional protocols, this nanocatalyst offers advantages such as high catalytic efficiency, superior yields, short reaction duration, inexpensive nature, operational simplicity, reusability, and environmental benignity. The findings underscore the potential of nanostructured catalysts in advancing green synthetic strategies.

1 Introduction

4*H*-Pyrano[2,3-*c*]pyrazoles and their derivatives represent a significant class of nitrogen-containing heterocyclic scaffolds with significant pharmacological relevance, demonstrating a broad spectrum of biological properties such as anti-inflammatory,[1] antimicrobial,[2,3] anticancer,[4,5] antiviral,[6] analgesic,[7] antibacterial,[8] antifungal, antimalarial,[9] and antioxidant properties[10] (Fig. 1). They also act as vasodilators and potent antiplatelet agents,[11] in addition to exhibiting hypoglycemic and hypotensive effects.[12]

Certain pyrazole derivatives show high affinity toward A_1 and A_2A adenosine receptors and display molluscicidal activity.[13,14] They are further investigated as Chk1 kinase inhibitors,[15] cognitive enhancers, and therapeutic agents for neurodegenerative conditions including Down's syndrome, AIDS-related dementia, amyotrophic lateral sclerosis (ALS), and Alzheimer's disease.[16,17] Moreover, they have applications in the management of schizophrenia and Huntington's disease, making them valuable scaffolds in drug design.[18] However, traditional methods for synthesizing pyrazoles suffer from several drawbacks, including extended reaction times, low yields, the use of hazardous and volatile solvents, high-temperature reflux conditions, energy-consuming processes like microwave-sonication, expensive catalysts, and tedious column purification steps.[19,20]

These issues result in environmental burdens, health risks, and increased processing costs. As a result, there is a growing need for greener and more efficient synthetic routes that minimize environmental impact while improving reaction efficiency.[21,22] In this regard, heterogeneous catalysis has emerged as a key strategy for sustainable synthesis.[23]

Zinc oxide (ZnO), a widely used semiconductor, has shown promising catalytic activity. Still, its application is limited by a minimal surface area, particle agglomeration, limited activity under solvent-free conditions, possible Zn^{2+} leaching, poor selectivity in complex reactions, and lacks structural tunability for shape-selective catalysis.[24,25] To overcome these limitations, several modification strategies have been employed, including surface chelation,[26] derivatization,[27] surface coating,[28] platinization,[29] and selective element doping.[30]

Among these, doping with lanthanum has proven particularly effective, due to its large ionic radius and +3 charge, which induce lattice distortion and oxygen vacancies-enhancing active site density and catalytic activity. La^{3+} suppresses grain growth, increases surface area, and improves structural integration without forming secondary phases. Its incorporation imparts Lewis acid-base bifunctionality, thermal stability, and excellent

[a]*Department of Chemistry, MVP's K. R. T. Arts, B. H. Commerce and A. M. Science (K. T. H. M.) College, Savitribai Phule Pune University, Shivaji Nagar, Nashik - 422 002, Maharashtra, India. E-mail: hslabhade13@gmail.com*

[b]*Department of Chemistry, VPM's B.N. Bandodkar College of Science (Autonomous), Jnanadweepa, Chedani Bunder Road, Thane (W) - 400 601, Maharashtra, India*

[c]*Department of Chemistry, Kr.V.N. Naik Shikshan Prasarak Sanstha's Arts, Commerce and Science College, Savitribai Phule Pune University, Canada Corner, Nashik - 422 002, Maharashtra, India*

† Electronic supplementary information (ESI) available. See DOI: https://doi.org/10.1039/d5ra02788h

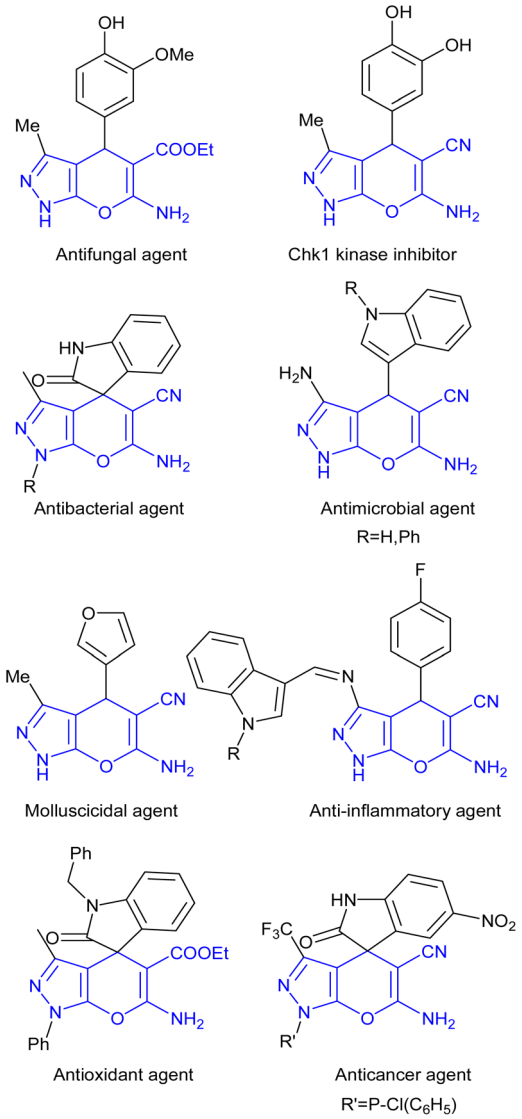

Fig. 1 Schematic representation of 4*H*-pyrano[2,3-*c*] pyrazole-based biologically active derivatives.

reusability, making it superior to many transition or rare-earth alternatives in multistep organic transformations.[31] Additionally, silver coating improves photocatalytic efficiency by enhancing charge separation, increasing conductivity, and expanding the surface area and porosity.[32]

The dual modification of ZnO with lanthanum and silver (Ag/La-ZnO) significantly improves selectivity, thermal and chemical stability, and overall catalytic performance. These nanoparticles facilitate solvent-free synthesis with excellent yields, shorter reaction times, minimal waste, ease of recovery, and straightforward product isolation-making them highly suitable for sustainable organic transformations.[33] Their application in pyrazole construction aligns with key green chemistry principles and promotes environmentally conscious synthetic approaches.

Accordingly, the present work investigates Ag/La-ZnO nanocatalyst assisted multicomponent synthesis of 4*H*-pyrano[2,3-*c*] pyrazoles under solvent-free grinding conditions, emphasizing its catalytic performance, operational ease, and environmental compatibility.

2 Experimental

2.1 Materials and instrument

All reagents, including lanthanum nitrate hexahydrate ($La(NO_3)_3 \cdot 6H_2O$), zinc nitrate hexahydrate ($Zn(NO_3)_2 \cdot 6H_2O$), silver nitrate, polyethylene glycol, sodium hydroxide, various aromatic aldehydes (labelled a–m), hydrazine hydrate, malononitrile, and ethyl acetoacetate, were of analytical grade and procured from commercial suppliers. These were used without further purification. Reaction progress was tracked by thin-layer chromatography (TLC) technique using silica gel 60 F254 plates. The synthesized Ag/La-ZnO nanoparticles were characterized using a range of techniques. X-ray diffraction (XRD) analysis was carried out using a Bruker D8 Advance diffractometer with Cu Kα radiation ($\lambda = 1.54$ Å). Field emission scanning electron microscopy (FESEM) and energy-dispersive X-ray spectroscopy (EDAX) were carried out on a Hitachi SU8010 microscope. High-resolution transmission electron microscopy (HRTEM) and selected area electron diffraction (SAED) analyses were conducted on a JEOL JEM-2100 microscope. Specific surface area measurements were obtained *via* N_2 physisorption using a Microtrac BEL BELSORP-max instrument. X-ray photoelectron spectroscopy (XPS) was recorded using an ESCA Omicron spectrometer equipped with a Mg Kα X-ray source ($h\nu = 1253.6$ eV). Melting points were measured in open capillary tubes and

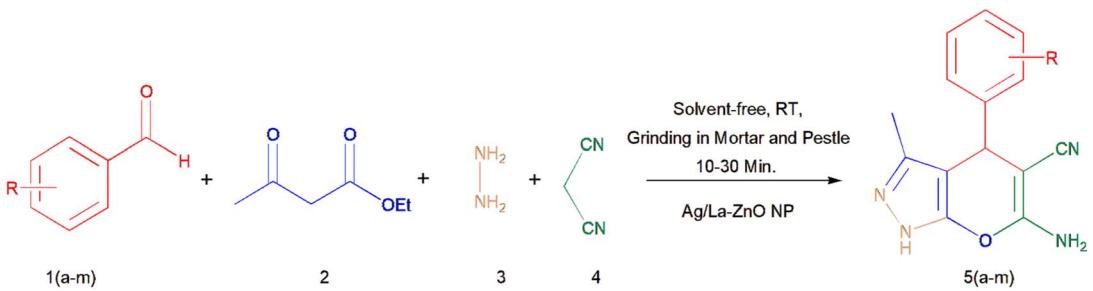

Scheme 1 Schematic representation of the solvent-free, four-component synthesis of 4*H*-pyrano[2,3-*c*]pyrazoles using aryl aldehydes, ethyl acetoacetate, malononitrile, and hydrazine hydrate *via* grinding in a mortar and pestle using the Ag/La-ZnO nanocatalyst.

are reported without correction. Infrared (IR) spectra were performed on a Thermo Nicolet iS50 spectrometer using KBr pellets. Mass spectra were acquired using a MALDI-TOF Synapt XS HD instrument. ^{1}H and ^{13}C NMR analysis carried on a Bruker Avance Neo 500 MHz spectrometer in $CDCl_3$ or DMSO-d_6 with tetramethylsilane (TMS) as the internal standard.

2.2 Synthesis of Ag/$La_{1-x}Zn_xO$ nanoparticles

$La_{1-x}Zn_xO$ nanoparticles (x = 0.01, 0.03, 0.05, and 0.07) were synthesized *via* a chemical precipitation method. In a typical procedure, stoichiometric amounts of zinc nitrate and a lanthanum precursor were dissolved in deionised water, succeeded by the dropwise introduction of sodium hydroxide solution under magnetic agitation at 120 °C. The pH was adjusted to 12, and the obtained white precipitate was further stirred for 2 h at 200 °C and then allowed to settle. The supernatant was decanted, and the precipitated solid was isolated *via* filtration and successively washed with deionized water followed by ethanol and then dried at 110 °C for 24 h. After drying the precipitate was subjected to grinding in an agate mortar and calcined at 800 °C for 4 h in a muffle furnace.[34–37]

For silver coating, the previously prepared $La_{1-x}Zn_xO$ nanoparticles were dispersed in deionised water and magnetically stirred for 30 minutes. A calculated amount of $AgNO_3$ (3.04 g per gram of La-ZnO), based on geometric and density estimations, was then introduced gradually under continuous stirring to achieve a uniform 4–5 nm silver shell. Polyethylene glycol was added as a stabilising agent to prevent agglomeration during the coating process. The suspension was loaded into a Teflon lined stainless-steel autoclave and thermally treated in an oven at 120 °C for 12 h. Resulting black Ag-coated $La_{1-x}Zn_xO$ nanoparticles were isolated by filtration, cleaned with deionized water and ethanol, then dried at 110 °C for 24 h. Finally, the product was subjected to calcination at 800 °C for 2 h. The resulting Ag/$La_{1-x}Zn_xO$ nanomaterial was employed as a catalyst in the preparation of pyrazole derivatives.[38,39]

2.3 General protocol for the synthesis of pyrazole derivatives

Following the successful synthesis and characterization of the catalyst, attention was directed toward evaluating its catalytic efficiency in a four-component, one pot condensation reaction of pyrazole synthesis. In this process, a combination of aryl aldehyde (**1a–m**, 1 mmol), ethyl acetoacetate (2, 1 mmol), hydrazine hydrate (3, 1 mmol), malononitrile (4, 1 mmol) and Ag/La-ZnO nanoparticles was ground for 10–25 minutes using a mortar and pestle (Scheme 1).[40] The advancement of the reaction was tracked using thin-layer chromatography (TLC) with a combination of ethyl acetate and *n*-hexane (60 : 40). After the reaction was complete, the mixture was allowed to cool to room temperature and the nanocatalyst was separated by gravity filtration. The crude pyrazole product present in the filtrate was then recrystallized from hot ethanol, affording the pure compound in good yield. The resulting pyrazole derivative (**5a–m**) was characterized by its melting point as well as various spectral data, including ^{1}HNMR, ^{13}CNMR, FTIR, and MS.

3 Result and discussion

3.1 Characterization of Ag/La-ZnO nanocatalyst

3.1.1 FTIR. The FTIR spectrum of Ag/La-ZnO nanoparticles reveals characteristic absorption bands corresponding to specific functional groups and metal–oxygen interactions. A prominent band observed near 500 cm^{-1} is attributed to the Zn–O stretching vibration, confirming the formation of zinc oxide bonds.[37] Weak bands observed near 1384 cm^{-1} and 1630 cm^{-1} are ascribed to the symmetric and asymmetric stretching modes of carboxylate or carbonate species, likely originating from residual precursors or atmospheric CO_2 adsorption. These features are commonly observed in metal oxide nanomaterials and do not indicate the presence of organic ligands in the final structure.[41] The incorporation of La and Ag into the ZnO matrix results in a marked reduction in the intensity of these carboxylate-related bands, suggesting their involvement in modifying the structural framework of the nanocomposite.[42] A broad absorption band appearing in the region of 3500–4000 cm^{-1} is assigned to the O–H stretching vibrations of physically adsorbed water molecules on the nanoparticle surface.[43,44] The FTIR spectrum of the 1st cycle Ag/La-ZnO sample exhibited minor additional peaks attributed to adsorbed pyrazole product, likely retained during catalyst

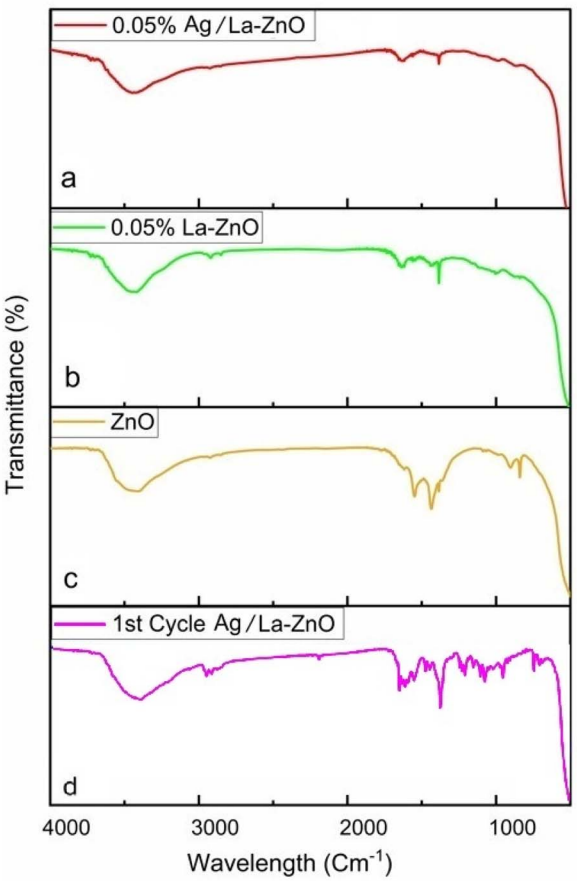

Fig. 2 FTIR spectra of undoped ZnO, La-ZnO, and Ag/La-ZnO and 1st cycle Ag/La-ZnO nanocatalysts.

Table 1 The XRD data for 0.05% Ag/La-ZnO nanocatalyst

Sr. no.	2θ	Miller indices h	k	l	d_{XRD} (Å)	d_{JCPDS}-36–1451 (Å)	Rel. peak intensity XRD	Rel. peak intensity JCPDS
1	31.87	1	0	0	2.8053	2.8143	59.4	57
2	34.53	0	0	2	2.5949	2.6033	43.7	44
3	36.36	1	0	1	2.4687	2.4759	100	100
4	47.64	1	0	2	1.9070	1.9111	21.4	23
5	56.68	1	1	0	1.6224	1.6347	32.7	32
6	62.95	1	0	3	1.4751	1.4771	25.1	29
7	66.44	2	0	0	1.4058	1.4071	4.2	4
8	68.03	1	1	2	1.3768	1.3781	17.5	23
9	69.18	2	0	1	1.3567	1.3582	8.5	11

Table 2 Structural parameters of undoped ZnO, 0.05% La-ZnO, 0.05% Ag/La-ZnO and 1st cycle 0.05% Ag/La-ZnO determined by XRD

Sr. no.	Catalyst	Peak position 2θ (°)	FWHM (β) (°)	Average crystal size (D) (nm)	Lattice parmeter (Å) $a = b$	c	a/c ratio	Unit cell volume (Å)^3	d-Value (Å)	Dislocation density (δ) (m^{-2})	Micro-strain (10^{-3})
1	Undoped ZnO	36.356	0.261	32.05	3.2409	5.1931	0.6241	47.2366	2.4691	1.08×10^{15}	3.11
2	La-ZnO	36.357	0.298	27.5	3.2379	5.1856	0.6244	47.0814	2.4666	1.34×10^{15}	3.48
3	Ag/La-ZnO	36.376	0.186	52.17	3.2382	5.1869	0.6243	47.1026	2.4669	1.89×10^{16}	2.36
4	1st cycle Ag/La-ZnO	36.354	0.231	36.07	3.2399	5.1899	0.6243	47.1798	2.4682	8.09×10^{14}	2.81

recovery. Importantly, the characteristic bands of the catalyst remained intact, indicating preservation of its structural integrity and morphology after reuse. These observations provide insight into the surface interactions and structural modification induced by dopant incorporation (Fig. 2).

3.1.2 XRD. The X-ray diffraction (XRD) analysis of Ag/La-ZnO nanoparticles exhibited distinct peaks at 2θ values of 31.87°, 34.53°, 36.36°, 47.64°, 56.68°, 62.95°, 66.44°, 68.03°, and 69.18°, corresponding to the (100), (002), (101), (102), (110), (103), (200), (112), and (201) crystal planes, respectively (Table 1). These diffraction peaks match well with the Joint Committee on Powder Diffraction Standards (JCPDS) card no. 36-1451, confirming the formation of a hexagonal wurtzite ZnO.[37] The calculated lattice parameters were $a = b = 3.238$ Å and $c = 5.1869$ Å, and the material was assigned to the $P6_3mc$ space group. The crystallite size (D) for nanoparticle samples is estimated using the Debye–Scherrer formula as $D = K\lambda/\beta\cos\theta$, where λ represented the wavelength of the X-ray radiation (CuKα = 1.5406 Å), and K was a constant with a value of 0.89, width at half maximum height was denoted as β, while θ referred to the diffracting angle.[45] Upon doping with La^{3+}, a slight shift of ZnO diffraction peaks to higher 2θ values was observed, indicative of La^{3+} substitution at Zn^{2+} lattice sites. The decrease in crystallite size, lattice volume, and unit cell parameters is attributed to lattice distortion induced by ionic radius differences ($La^{3+} = 116$ pm *vs.* $Zn^{2+} = 74$ pm), suggesting effective interstitial substitution and reduced crystal growth rate.[42] Following Ag coating, the XRD peaks exhibited further shifts to higher 2θ angles along with a reduction in intensity. Additionally, three new peaks at $2\theta = 38.20°$, 44.40°, and 64.52° were detected, corresponding to the (111), (200), and (220) planes of metallic silver, confirming the successful deposition of Ag onto La-ZnO[46] (Table 2). The introduction of Ag led to a slight increase in crystallite size and induced lattice defects, as reflected by the increased dislocation density, which may positively influence catalytic activity. The sharp and intense diffraction peaks confirmed the high crystallinity and structural integrity of the synthesized Ag/La-ZnO nanomaterials. The diffraction pattern of the reused catalyst retained all characteristic peaks at their original 2θ positions, indicating that the overall crystalline phase and structure remained intact after multiple catalytic cycles. However, a reduction in crystallite size to 36.07 nm and a slight increase in microstrain were observed, suggesting minor microstructural changes likely due to surface stress or particle fragmentation without affecting the bulk phase stability[47,48] (Fig. 3).

3.1.3 SEM. The SEM micrographs of Ag/La-ZnO nanoparticles reveal a crystalline, uniformly distributed morphology, with particles exhibiting varied shapes and sizes (Fig. 4). A degree of agglomeration is evident, which is commonly observed in nanoscale materials due to high surface energy and van der Waals forces. Occasional formation of larger particles from smaller ones is indicative of Ostwald ripening.[49]

3.1.4 EDAX – elemental mapping. The energy-dispersive X-ray analysis (EDAX) and elemental mapping confirmed the elemental composition of the synthesized nanocatalyst, validating the exitance of La and Ag without any detectable impurities[50] (Fig. 5 and 6). The observed lanthanum content closely

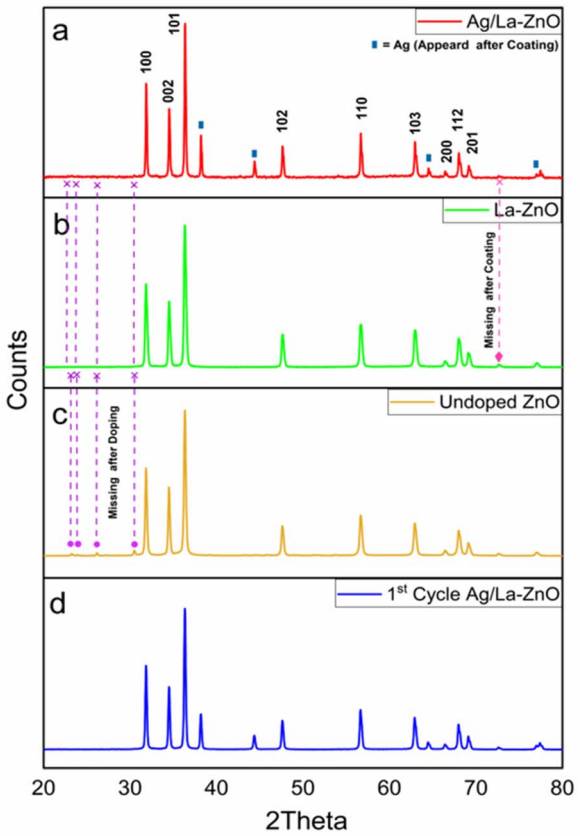

Fig. 3 The XRD pattern of (a) Ag/La-ZnO, (b) La-ZnO, (c) undoped ZnO, (d) 1st cycle Ag/La-ZnO nanocatalyst.

matched the nominal stoichiometry, indicating consistency with the targeted 0.05% Ag/La-ZnO formulation. These results affirm the successful doping and coating of the ZnO matrix along with the overall compositional homogeneity of the nanomaterial.

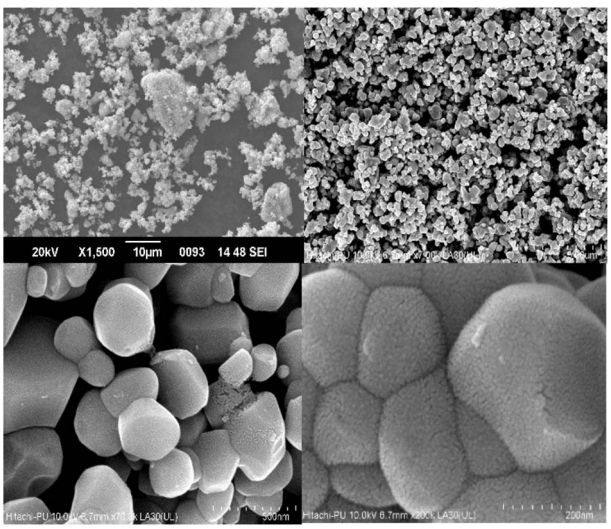

Fig. 4 SEM analysis of 0.05% Ag/La-ZnO nanoparticles.

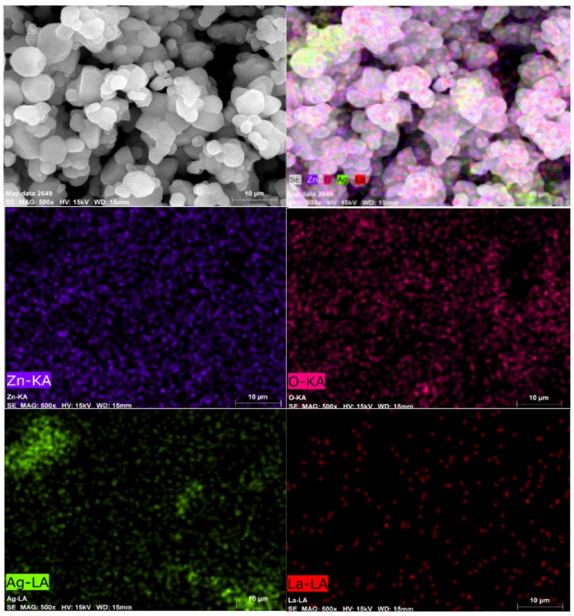

Fig. 5 Elemental mapping of Ag/La-ZnO nanoparticles.

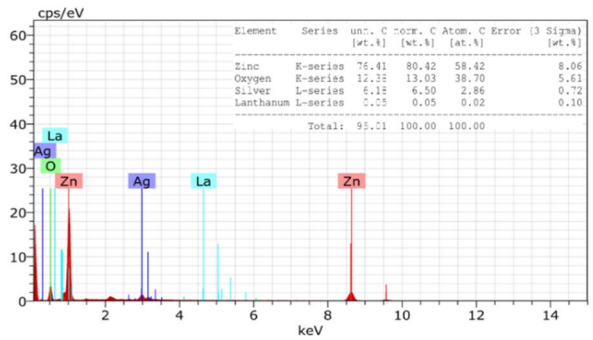

Fig. 6 EDAX spectrum of Ag/La-ZnO nanoparticles.

3.1.5 HRTEM – SAED. The particle size distribution method, applied to HRTEM images using a calibrated scale, revealed that the Ag/La-ZnO nanoparticles exhibit an average particle diameter of 30.8 ± 1.2 nm, indicating uniformity in size and morphology. The corresponding selected area electron diffraction (SAED) pattern confirmed the polycrystalline nature of the sample, with distinct diffraction rings indexed to the (100), (002), (101), (102), and (110) planes, consistent with a hexagonal wurtzite ZnO structure. La doping and Ag surface modification are likely responsible for inducing lattice strain, resulting in slight shifts in diffraction features. Variation in ring intensity may be attributed to electron scattering from both the La-ZnO core and Ag shell, consistent with the core–shell architecture. The HRTEM and SAED findings show excellent correlation with the XRD results, further validating the structural characteristics of the nanomaterial[51] (Table 3 and Fig. 7). Bright-field and dark-field (BF–DF) imaging additionally revealed notable nanoparticle agglomeration, consistent with surface energy-driven clustering phenomena (Fig. 8).

Table 3 SAED parameters for 0.05% Ag/La-ZnO

Ring number	Experimental ring diameter (nm^{-1})	Converted radius (nm^{-1}) (diameter/2)	Calculated *d*-spacing (Å) (1/*R*)	Standard *d*-spacing (JCPDS-36-1451) (Å)	Corresponding (*hkl*) plane
1	7.175	3.588	2.786	2.81	100
2	8.120	4.060	2.463	2.60	002
3	11.318	5.659	1.767	1.91	101
4	14.227	7.113	1.406	1.62	102
5	18.249	9.124	1.096	1.38	110

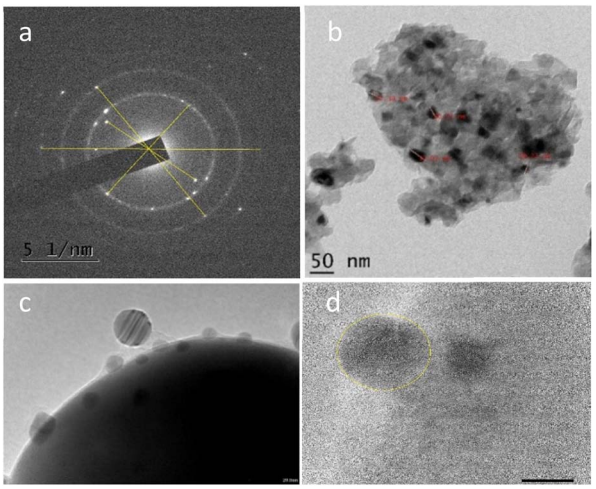

Fig. 7 (a) SAED image, (b–d) HR-TEM images of Ag/La-ZnO nanoparticles.

3.1.6 BET surface area. The N_2 adsorption–desorption isotherms of Ag/La-ZnO nanoparticles exhibit a Type IV isotherm with an H3 hysteresis loop, characteristic of mesoporous materials possessing slit-like pores.[52,53] This profile is typically associated with aggregates of plate-like particles and suggests a heterogeneous surface with a broad distribution of pore sizes. Brunauer–Emmett–Teller (BET) analysis revealed a specific surface area of 2.4862 $m^2\ g^{-1}$, a monolayer adsorption capacity (V_m) of 0.5712 $cm^3\ g^{-1}$, and a BET constant (*C*) of 59.888. The high *C* value indicates strong adsorbate–absorbent interactions, consistent with the presence of a non-uniform surface and multilayer adsorption behavior. The total pore volume at a relative pressure (p/p_0) of 0.990 was measured to be 0.020869 $cm^3\ g^{-1}$, and the average pore diameter was found to be 33.577 nm, indicating the coexistence of mesopores and interparticle voids.[54] Barrett–Joyner–Halenda (BJH) analysis provided further insights into the pore structure, yielding an average pore volume of 0.020663 $cm^3\ g^{-1}$, a peak pore radius of 9.46 nm, and a BJH surface area of 2.0731 $m^2\ g^{-1}$ with hierarchical pore system, consistent with mesoporous character (Fig. 9). Although the specific surface area is relatively modest, the uniform mesoporosity facilitates efficient mass transfer and exposes a greater number of catalytically active sites. This structural feature is particularly advantageous under solvent-free grinding conditions, where enhanced diffusion and increased surface accessibility directly support observed catalytic efficiency in the multicomponent reaction. The observed H3 hysteresis loop indicates delayed desorption, which may be attributed to pore connectivity and surface roughness. This behaviour is advantageous for applications requiring controlled adsorption and release, such as heterogeneous catalysis,[55] gas sensing,[55] controlled drug delivery, and adsorption-based separations.[56]

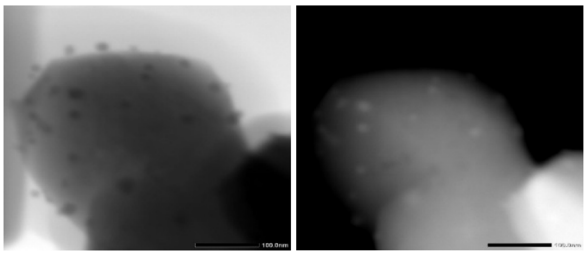

Fig. 8 Bright field-dark field images of Ag/La-ZnO Nanoparticles.

3.1.7 XPS. The XPS analysis confirms the chemical composition and elemental incorporation of La^{3+} and Ag on ZnO nanoparticles, distinguishing surface *vs.* bulk composition as XPS primarily probes the top 1–10 nm. The Ag 3d spectrum exhibits peaks at 368.2 eV (Ag^0) and 373.5 eV (Ag^+), confirming both metallic and oxidized silver, suggesting partial oxidation due to environmental exposure or surface interactions.[57,58] The La 3d peaks in XPS confirm La^{3+} in an oxidized state, indicating successful doping.[59] Binding energy shifts in Zn $2p_{1/2}$ appear around 1044 eV, while Zn $2p_{3/2}$ is near 1020.56 eV suggesting charge redistribution between Zn^{2+} and La^{3+}, affecting electronic properties.[60,61] The O 1s spectrum, with a peak at 529.46 eV (lattice oxygen, O^{2-}), confirms increased defect density due to La doping, enhancing charge carrier dynamics.[62] (Fig. 10) Oxygen vacancies and hydroxyl groups suggest potential chemical bonding interactions that influence catalytic efficiency. The Ag coating, evident from Ag^0 and Ag^+ species, suggests strong interfacial interactions that may enhance plasmonic and electronic effects.[63]

3.2 Synthesis of pyrazole derivatives

To achieve optimal results, the reaction conditions underwent careful optimization. Benzaldehyde, hydrazine hydrate, ethyl acetoacetate, and malononitrile were utilized as model substrates for the synthesis of **5a**.

3.2.1 Effect of La doping. Initially, a control experiment conducted without the catalyst demonstrated an incomplete reaction even after 5 hours. To explore the impact of La doping and Ag coating on catalytic activity, Ag/La-ZnO nanoparticles

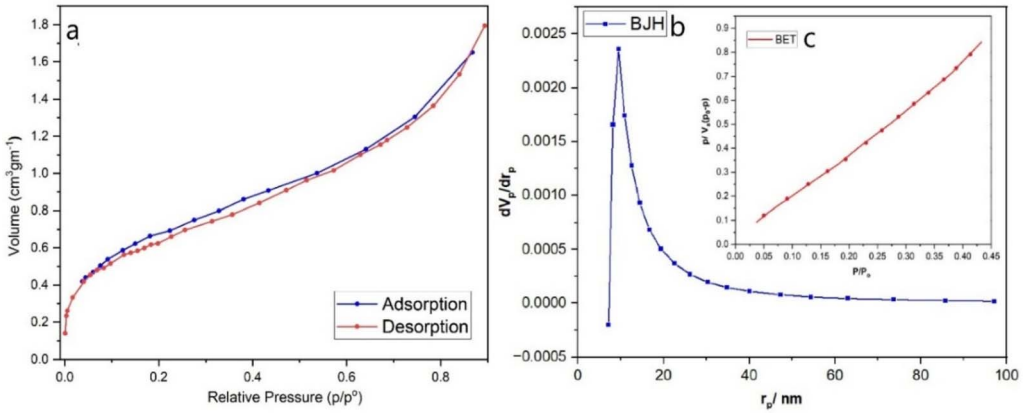

Fig. 9 (a) Adsorption-desorption isotherm, (b) BJH plot, (c) BET plot.

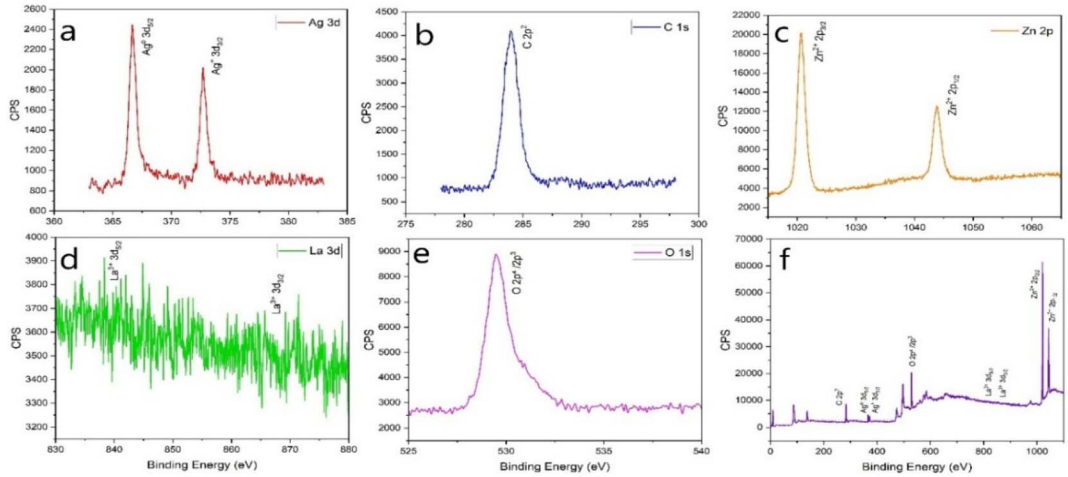

Fig. 10 XPS images of Ag/La-ZnO nanoparticle: (a) Ag 3d spectra, (b) C 1s spectra, (c) Zn 2p spectra, (d) La 3d spectra (e) O 1s spectra and (f) XPS survey spectra.

were synthesized with La concentrations of 0.01%, 0.03%, 0.05%, and 0.07%. The 0.05% Ag/La-ZnO catalyst achieved the highest yield with the shortest reaction time in model reaction, while further doping showed no significant improvement. A comparison of 0.05% La-ZnO and 0.05% Ag/La-ZnO revealed that Ag coating, through enhanced surface area, facilitated a higher yield of 94% with a reduced reaction time of 10 minutes (Table 4).

Table 4 Optimization of dopant concentration

Entry	Catalyst	Condition	Time (min)	Yield (%)
1	—	Reflux, H_2O	300	67 (ref. 85)
2	Nano ZnO	H_2O, 70 °C	60	94 (ref. 84)
3	0.05% La-ZnO	Solvent free	60	71
4	0.01% Ag/La-ZnO	Solvent free	40	76
5	0.03% Ag/La-ZnO	Solvent free	30	86
6	**0.05% Ag/La-ZnO**	**Solvent free**	**10**	**94**
7	0.07% Ag/La-ZnO	Solvent free	10	93

Table 5 Optimization of catalyst loading

Entry	Catalyst (mg)	Time (min)	Yield (%)
1	30	60	74
2	50	45	81
3	100	20	87
4	**120**	**10**	**94**
5	150	10	94

Table 6 Solvent effect on reaction for the synthesis of **5a** product in the presence of 0.05% Ag/La-ZnO catalyst

Entry	Solvent	T (°C)	Time (min)	Yield (%)
1	**Solent free**	**r.t**	**10**	**94**
2	EtOH	r.t	10	92
3	MeOH	r.t	10	92
4	$CHCl_3$	r.t	30	77
5	Toluene	r.t	40	72
6	DMF	r.t	40	75
7	CH_3CN	r.t	50	68

Table 7 Ag/La-ZnO nanoparticles catalysed synthesis of pyrazole derivatives[a]

Entry	ArCHO **1a–m**	Product **5a–m**	Time (min)	Yield (%)	M. P (°C) observed	M. P (°C) reported
5a	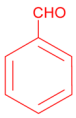	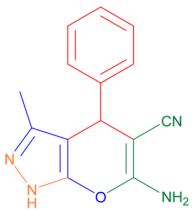	10	94	245	243–245 (ref. 65)
5b	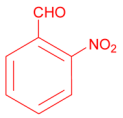	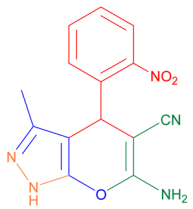	10	88	242	242–244 (ref. 67)
5c	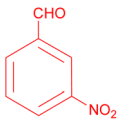	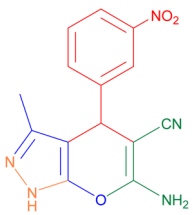	10	95	214	214–216 (ref. 84)
5d		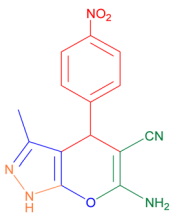	10	93	195	193–195 (ref. 65)
5e	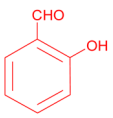	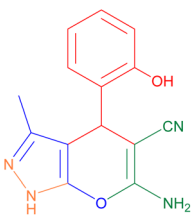	20	83	210	209–211 (ref. 69)
5f	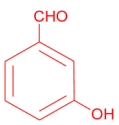	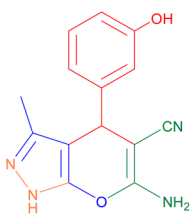	20	84	235	236–238 (ref. 70)
5g	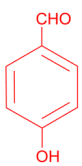	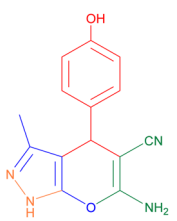	20	82	225	222–224 (ref. 65)

Table 7 (*Contd.*)

Entry	ArCHO **1a–m**	Product **5a–m**	Time (min)	Yield (%)	M. P (°C) observed	M. P (°C) reported
5h	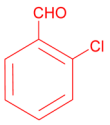	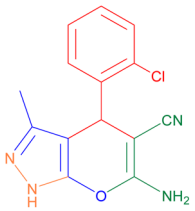	15	88	245	245–246 (ref. 65)
5i		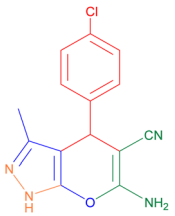	15	86	235	233–235 (ref. 84)
5j		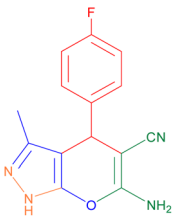	10	92	167	167–168 (ref. 66)
5k		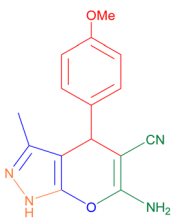	25	82	212	211–212 (ref. 84)
5l	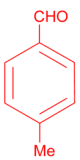	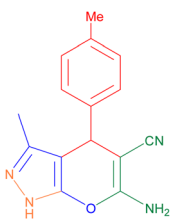	25	84	206	206–208 (ref. 84)
5m	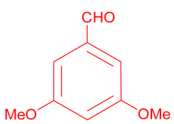	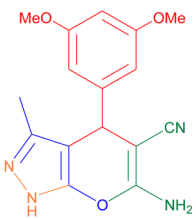	25	79	195	193–195 (ref. 66)

[a] Reaction condition: Aryl aldehyde (**1a–m**,1 mmol), ethyl acetoacetate (2, 1 mmol), hydrazine hydrate (3, 1 mmol), malononitrile (4, 1.0 mmol) in the presence of 0.05% Ag/La-ZnO nanocatalyst (120 mg) at ambient room temperature in solvent-free grinding conditions.

3.2.2 Effect of catalyst loading. Catalyst loading plays a critical role in governing reaction kinetics and efficiency. As shown in Table 5, increasing the catalyst amount from 30 mg to 120 mg significantly reduced the reaction time from 60 minutes to 10 minutes while increasing the yield from 74% to 94%. This improvement can be attributed to the greater availability of active catalytic sites, which accelerates the adsorption and activation of reactant molecules under grinding conditions.

However, further increasing the catalyst amount to 150 mg did not improve the yield or reduce the reaction time, indicating that beyond an optimal threshold, the reaction reaches a saturation point where additional catalyst offers no kinetic advantage. This plateau suggests that 120 mg is the most efficient catalyst loading for this transformation, balancing both catalytic performance and material economy (Table 5).

3.2.3 Effect of solvent. The solvent effect was evaluated to understand the influence of reaction medium polarity on the catalytic efficiency of Ag/La-ZnO (Table 6). Remarkably, the reaction proceeded most efficiently under solvent-free conditions, affording the desired product in 94% yield within 10 minutes. The enhanced performance in the absence of solvent may be attributed to higher local concentrations of reactants, improved contact with the catalyst surface, and elimination of solvent competition for active sites. Polar protic solvents such as ethanol and methanol provided slightly lower but still acceptable yields of 92%, likely due to their hydrogen-bonding ability partially stabilizing intermediates. In contrast, polar aprotic solvents (DMF, CH_3CN) and nonpolar solvents (toluene, $CHCl_3$) led to extended reaction times and decreased yields (68–77%). These media may dilute reactants and interfere with adsorption onto the catalyst surface, thereby reducing catalytic efficiency. These results reinforce the green and operationally simple advantage of solvent-free grinding conditions in this methodology.

3.2.4 Effect of electronic substituents on catalyst efficiency. The substrate scope was evaluated using various substituted aromatic aldehydes, and the results are summarized in Table 7. The electronic and steric nature of the substituents on the aryl ring significantly influenced the reaction efficiency. Aromatic aldehydes bearing electron-withdrawing groups (*e.g.*, $-NO_2$, –Cl) exhibited higher reactivity and shorter reaction times, attributed to their increased carbonyl electrophilicity, which is further activated by the Lewis acidic Zn^{2+} sites on the Ag/La-ZnO catalyst during the Knoevenagel condensation. This activation promotes faster formation of the intermediate and facilitates subsequent Michael addition and cyclization steps. In contrast, aldehydes with electron-donating groups (*e.g.*, –OMe, –Me) showed reduced reactivity and lower yields due to decreased electrophilicity. Additionally, substrates containing hydroxyl groups required extended reaction times and gave moderate yields, likely due to intramolecular hydrogen bonding which hamper catalyst–substrate interactions hindering reactivity.[64]

3.2.5 Reusability of catalyst. Catalyst reusability was assessed by recovering it after the reaction, washing with acetone, and drying at 200 °C. The catalyst was reused in the model reaction for four consecutive cycles, maintaining high activity with minimal loss in performance. This aspect is crucial from both economic and environmental perspectives, as catalyst stability directly impacts process sustainability. Yields in the second, third, and fourth runs were 92%, 87%, and 85%, respectively-comparable to the initial yield of 94%, demonstrating the catalyst's robustness and recyclability (Fig. 11).

3.2.6 Comparative evaluation of catalytic efficiency. Furthermore, a comparative study was conducted to showcase the effectiveness of the synthesized Ag/La-ZnO nanocatalyst in contrast to other catalysts previously reported for the synthesis of pyrazole scaffolds (Table 8). The findings highlighted the superiority of the current method over earlier reported approaches in terms of catalyst quantity, product yield, and reaction duration.

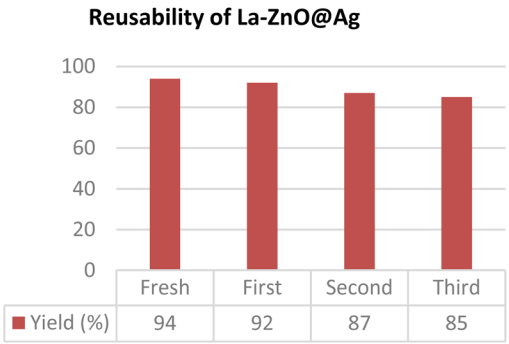

Fig. 11 Reusability of Ag/La-ZnO nanocatalyst.

3.2.7 Proposed plausible reaction mechanism. The plausible mechanism for the Ag/La-ZnO catalyzed synthesis of 4*H*-pyrano[2,3-*c*]pyrazoles involves initial formation of pyrazolone *via* condensation of ethyl acetoacetate with hydrazine, activated by the Lewis acidic Zn^{2+} and basic La–O^- sites. Simultaneously, a Knoevenagel condensation between aldehyde and malononitrile forms the arylidene intermediate. Michael addition of pyrazolone to this intermediate, followed by intramolecular cyclization and tautomerism, yields the final product. The La^{3+} dopant enhances charge separation and catalytic efficiency, while the Ag shell promotes electron transfer, collectively accelerating the multistep transformation (Fig. 12).

3.2.8 Spectral data of some pyrazole derivatives

3.2.8.1 6-Amino-2,4-dihydro-3-methyl-4-phenylpyrano[2,3-c] pyrazole-5-carbonitrile. Table 7 compound **5a**: White solid; mp 243–245 °C. IR (KBr, ν_{max}/cm^{-1}): 3369 and 3165 (NH), 2979 (C–H), 2192 (conj. CN), 1729 (C=O), 1 (ref. 64) 7 and 1595 (C=C), 1489, 1452, 1399, 1367, 1226, 1159, 1030, 744, 697, 542. δ_H (500 MHz, DMSO-d_6; *J* in Hz): 12.10 (1H, s, NH), 7.32 (2H, t, $J = 7.5$, ArH), 7.23 (1H, d, $J = 7.3$, ArH), 7.18–7.15 (2H, m, ArH), 6.85 (2H, br s, NH_2), 4.59 (1H, s, CH-pyrano), 1.78 (3H, s, CH_3). δ_C (500 MHz, DMSO-d_6): 160.9, 154.7, 144.4, 135.7, 128.5, 127.4, 126.8, 120.8, 97.7, 57.3, 36.2, 9.7. HRMS (ESI^+): *m*/*z* $[M + H]^+$ calcd for $C_{14}H_{13}N_4O_2$: 257.1038, found: 257.1448.

3.2.8.2 6-Amino-4-(2-hydroxyphenyl)-3-methyl-2,4-dihydropyrano [2,3-c] pyrazole-5-carbonitrile. Table 7 compound **5e**: White solid; mp 209–211 °C. IR (KBr, ν_{max}/cm^{-1}): 3444, 3415, 3347 (OH, NH), 2928 (C–H), 2186 (conj. CN), 1659 (C=O), 1613, 1534, 1487, 1403, 1313, 1266, 1228, 1182, 1150, 1049, 970, 893, 825, 767, 733, 697, 651, 623, 546, 492. δ_H (500 MHz, DMSO-d_6; *J* in Hz): 11.14 (1H, s, OH), 9.01 (1H, s, NH), 7.71 (1H, d, $J =$ 7.5 Hz, ArH), 7.41 (1H, m, ArH), 7.18 (1H, m, ArH), 7.04 (1H, m, ArH), 6.97 (1H, dd, ArH), 6.67 (2H, s, NH_2), 4.63 (1H, s, CH–pyrano), 1.96 (3H, s, CH_3). δ_C (500 MHz, DMSO-d_6): 160.2, 148.4, 130.9, 129.0, 127.7, 124.4, 123.5, 120.9, 116.6, 115.6, 105.0, 55.1, 28.7, 9.9. MS (HRMS, ESI^+): *m*/*z* $[M + H]^+$ calcd for $C_{14}H_{13}N_4O_3$: 269.0987, found: 269.0976.

Table 8 Comparative study of catalyst for the synthesis of pyrazole derivatives

Entry	Catalyst	Reaction condition	Time (min)	Yield (%)	Ref.
1	TEBA	H_2O; 90 °C	360–600	87–99	66
2	[bmim]OH	50–60 °C	300–600	84–96	67
3	Et_3N	EtOH; 50 °C; sonication	25–40	87–92	68
4	CMC-SO_3H	EtOH; 60 °C	35–60	70–92	69
5	NFS–PWA	EtOH; reflux	45–60	82–91	70
6	MorT	EtOH–H_2O; reflux	360–720	54–95	71
7	Montmorillonite K-10	EtOH/H_2O; r.t	300–480	80–91	72
8	$B(OH)_3$	Solvent-free; 70 °C	10–20	70–85	73
9	Sodium benzoate	H_2O; r.t	30–75	78–94	74
10	Nano-$TiO_2/H_{14}[NaP_5W_{30}O_{110}]$	EtOH; 50 °C; sonication	10–30	83–98	75
11	N_2H_4, cat. Piperazine	CMUI	40–60	89–93	76
12	$SnCl_2$	Microwave	10–20	60–88	77
13	Thiourea dioxide	H_2O; 80 °C	30–50	86–96	78
14	Sodium gluconate	H_2O; reflux	15–45	82–92	79
15	TBD-MSN	EtOH; reflux	30–50	84–95	80
16	$[Hmim]HSO_4$	Ethanol 50%, 50 °C	15–90	75–92	81
17	$Fe_3O_4@SiO_2$	EtOH/H_2O; 70 °C	20–40	80–94	82
18	Alumina	H_2O; reflux	35–75	61–90	83
19	Nano ZnO	H_2O; 70 °C	60–90	82–94	84
20	Ag/La-ZnO	Grinding; r.t	10–25	79–95	**This work**

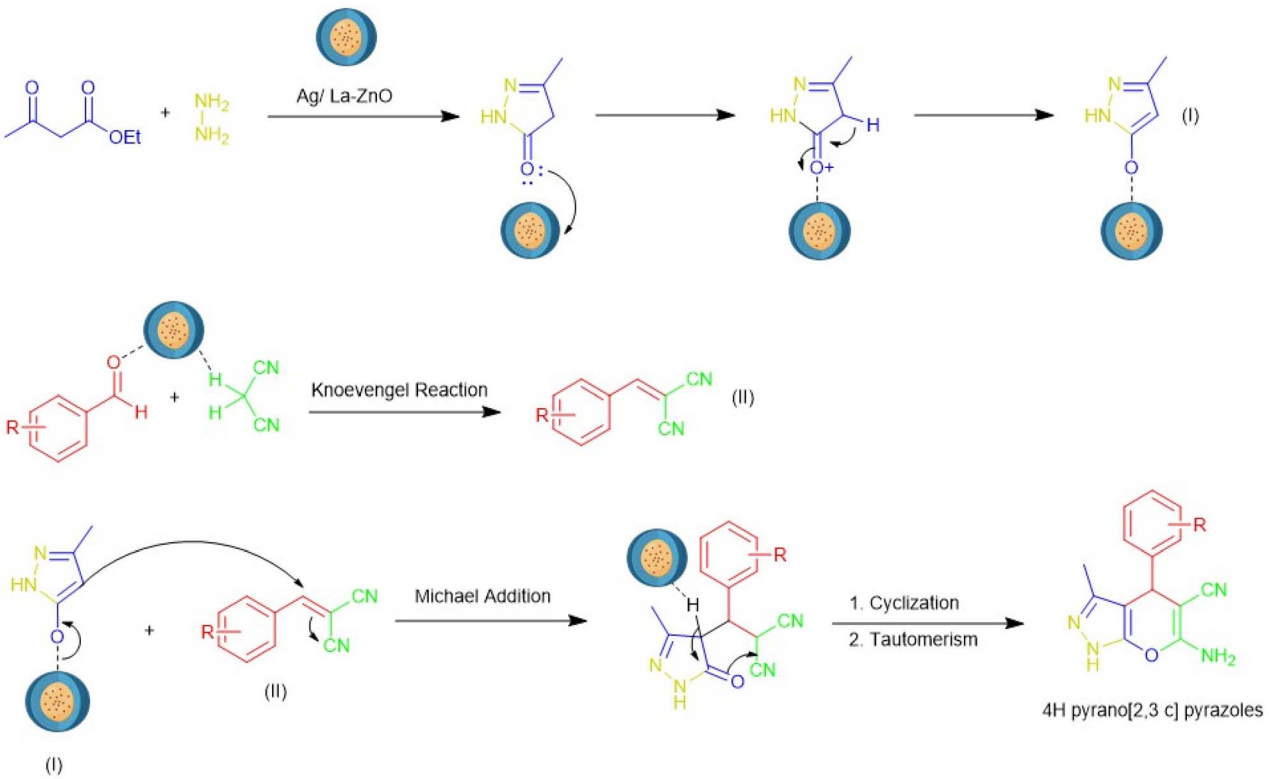

Fig. 12 Plausible mechanism for the Ag/La-ZnO nanoparticle catalyzed four-component synthesis of pyrazoles.

3.2.8.3 6-Amino-4-(3,5-methoxyphenyl)-3-methyl-2,4-dihydropyrano [2,3-c] pyrazole-5-carbonitrile. Table 7 compound **5m**: White solid; mp 193–195 °C. IR (KBr, ν_{max}/cm^{-1}): 3616, 3371, 3128 (NH, OCH_3), 2936, 2840 (C–H), 2184 (conj. CN), 1645 (C=O), 1596, 1512, 1492, 1400, 1346, 1252, 1168, 1137, 1021, 875, 812, 750, 678, 602, 568. δ_H (500 MHz, DMSO-d_6; J in Hz): 12.07 (1H, s, OH), 6.89 (1H, d, $J = 8.3$ Hz, ArH), 6.80 (2H, s, NH_2), 6.75 (1H, d, $J = 2.0$ Hz, ArH), 6.68 (1H, dd, $J = 8.2$, 2.0 Hz, ArH), 4.55 (1H, s, CH–pyrano), 3.73 (3H, s, OCH_3), 3.70 (3H, s, OCH_3), 1.82 (3H, s, CH_3). δ_C (500 MHz, DMSO-d_6): 160.7, 154.7, 148.5, 147.5, 136.9, 135.7, 120.9, 119.5, 111.7, 111.2, 97.7, 57.5, 55.5,

55.4, 35.8, 9.8. MS (HRMS, ESI^+): m/z $[M + H]^+$ calcd for $C_{16}H_{15}N_4O_4$: 313.1142, found: 313.1243.

3.2.8.4 6-Amino-4-(4-chlorophenyl)-3-methyl-2,4-dihydropyrano [2,3-c] pyrazole-5 carbonitrile. Table 7 compound **5i**: White solid; mp 233–235 °C. IR (KBr, ν_{max}/cm^{-1}): 3424, 3329 (NH), 2982, 2930 (C–H), 2193 (conj. CN), 1674 (C=O), 1604, 1467, 1410, 1339, 1259, 1212, 1179, 1144, 1060, 1035, 944, 856, 829, 681, 644, 576. δ_H (500 MHz, DMSO-d_6; J in Hz): 12.14 (1H, s, OH), 7.38 (2H, d, $J = 8.4$ Hz, ArH), 7.20 (2H, d, $J = 8.5$ Hz, ArH), 6.91 (2H, s, NH_2), 4.63 (1H, s, CH–pyrano), 1.83 (4H, s, CH_3). δ_C (500 MHz, DMSO-d) 160.6, 143.4, 131.3, 130.0, 129.4, 129.1, 128.5, 97.2, 56.8, 35.5, 9.7. MS (HRMS, ESI^+): m/z $[M + H]^+$ calcd for $C_{14}H_{12}ClN_4O_2$: 287.0637, found: 287.0627.

4 Conclusion

In this study, we successfully demonstrated the catalytic efficiency of lanthanide-doped and silver-coated zinc oxide (Ag/La-ZnO) nanocatalyst for the green, solvent-free synthesis of pyrazole derivatives. Lanthanide incorporation into the ZnO lattice, combined with Ag nanoparticle coating, significantly enhanced the catalyst's surface properties and reactivity. Extensive characterization using IR, XRD, SEM, and related techniques confirmed the structural integrity, excellent crystallinity, and uniform elemental distribution of the Ag/La-ZnO nanoparticles, supporting their suitability for catalytic applications. Optimization of reaction conditions and reusability studies further demonstrated the robustness and stability of the catalyst, with minimal loss in activity over multiple cycles. The developed system outperformed previously reported catalysts in terms of solvent-free condition, reusability, lower catalyst loading, shorter reaction time, higher yields, non-column purification and cost-effective nature highlighting its potential for practical use. Overall, this work presents a sustainable, one-pot, four-component catalytic approach for pyrazole synthesis, aligning with green chemistry principles and offering a promising platform for future applications in eco-friendly organic transformations.

Data availability

Data for this article are available at Zenedo at **https://doi.org/10.5281/zenodo.15256408**.

Author contributions

Hrishikesh Labhade: formal analysis, data curation, methodology, investigation, writing–original draft; Jaidip Wable, Amol Kategaonkar, Samin Shaikh: data curation, methodology; Sharad Gaikwad: validation, conceptualization, supervision, project administration, writing–review and editing.

Conflicts of interest

There are no conflicts to declare.

Acknowledgements

We extend our sincere gratitude to Prof. A. V. Borhade for his valuable suggestions and guidance. We also thank the Principals of KTHM College, Nashik, and B. N. Bandodkar College of Science, Thane, for providing access to the necessary laboratory facilities. The authors acknowledge DST-SAIF, Cochin, Kerala, and Panjab University's SAIF, Chandigarh, for providing spectral analysis support. We are also grateful to the CSIF, University of Calicut, Kerala, for facilitating BET surface area measurements.

Notes and references

1 P. L. Kumar, D. K. Aneja, G. K. Gupta, D. Kaushik and O. Prakash, *Eur. J. Med. Chem.*, 2012, **50**, 81–89.
2 P. H. Parikh, J. B. Timaniya, M. J. Patel and K. P. Patel, *J. Mol. Struct.*, 2022, **1249**, 131605.
3 M. Parshad, V. Verma and D. Kumar, *Monatsh. Chem.*, 2014, **145**, 1857–1865.
4 J. Wang, D. Liu, Z. Zheng, S. Shan, X. Han, S. M. Srinivasula, C. M. Croce, E. S. Alnemri and Z. Huang, *Proc. Natl. Acad. Sci. U. S. A.*, 2000, **97**, 7124–7129.
5 I. F. F. Nassar, H. El Feky, Z. K. Hamza, H. Abo-Salem and A. A.-H. Abdel-Rahman, *Egypt. J. Chem.*, 2022, **65**(132), 1489–1505.
6 A. K. Allayeh, A. H. El-boghdady, M. A. Said, M. G. A. Saleh, M. T. Abdel-Aal and M. G. Abouelenein, *Pharmaceuticals*, 2024, **17**, 198.
7 A. K. E.-D. El-Ansary, A. T. Taher, A. A. E.-H. El-Rahmany and S. El Awdan, *J. Am. Sci.*, 2014, **10**(10), 284–294.
8 M. Mamaghani, R. Hossein Nia and F. Shirini, *Med. Chem. Res.*, 2015, **24**, 3451–3457.
9 M. A. Shamsuddin, A. H. Ali, N. H. Zakaria, M. F. Mohammat, A. S. Hamzah, Z. Shaameri, K. W. Lam, W. F. Mark-Lee, H. K. Agustar, M. R. M. Abd Razak, J. Latip and N. I. Hassan, *Pharmaceuticals*, 2021, **14**, 1174.
10 S. P. Khare, T. R. Deshmukh, J. N. Sangshetti, V. M. Khedkar and B. B. Shingate, *Synth. Commun.*, 2019, **49**, 2521–2537.
11 S. N. Sirakanyan, M. Hrubša, D. Spinelli, P. Dias, V. Kartsev, A. Carazo, A. A. Hovakimyan, J. Pourová, E. K. Hakobyan, J. Karlíčková, S. Parvin, J. Fadraersada, K. Macáková, A. Geronikaki and P. Mladěnka, *J. Pharm. Pharmacol.*, 2022, **74**(6), 887–895.
12 M. Ramadan, A. A. Aly, L. E. A. El-Haleem, M. B. Alshammari and S. Bräse, *Molecules*, 2021, **26**, 4995.
13 V. Colotta, D. Catarzi, F. Varano, F. Melani, G. Filacchioni, L. Cecchi, L. Trincavelli, C. Martini and A. Lucacchini, *Il Farmaco*, 1998, **53**, 189–196.
14 F. M. Abdelrazek, P. Metz, O. Kataeva, A. Jäger and S. F. El-Mahrouky, *Arch. Pharm.*, 2007, **340**, 543–548.
15 N. Foloppe, L. M. Fisher, R. Howes, A. Potter, A. G. Robertson and A. E. Surgenor, *Bioorg. Med. Chem.*, 2006, **14**, 4792–4802.
16 S. Hameed, O. Babatunde, U. Salar, A. Jabbar, S. Chigurupati, M. Solangi, L. Atta, Z. Ul-Haq, F. Saleem, S. Bhatia, A. Al-Harrasi, M. Taha and K. M. Khan, *Future Med. Chem.*, 2022, **14**, 1507–1526.

17 S. Das, S. Akbar, B. Ahmed, R. P. Dewangan, M. K. Iqubal, A. Iqubal, P. Chawla, F. H. Pottoo and A. Joseph, *CNS Neurol. Disord.:Drug Targets*, 2022, **21**, 940–951.
18 S. K. Biswas and D. Das, *Mini-Rev. Org. Chem.*, 2022, **19**, 552–568.
19 A. D. Curzons, D. C. Constable and V. L. Cunningham, *Clean Prod. Process.*, 1999, **1**, 82–90.
20 D. R. Joshi and N. Adhikari, *J. Pharm. Res. Int.*, 2019, **28**, 1–18.
21 M. Himaja, D. Poppy and K. Asif, *Int. J. Res. Ayurveda Pharm.*, 2011, **2**, 1079–1086.
22 M. B. Gawande, V. D. B. Bonifácio, R. Luque, P. S. Branco and R. S. Varma, *ChemSusChem*, 2014, **7**, 24–44.
23 V. Polshettiwar and R. S. Varma, *Green Chem.*, 2010, **12**, 743–754.
24 L. T. T. Nguyen, L. T. H. Nguyen, A. T. T. Duong, B. D. Nguyen, N. Quang Hai, V. H. Chu, T. D. Nguyen and L. G. Bach, *Mater*, 2019, **12**, 1195.
25 M. Al Bitar, M. Khalil and R. Awad, *Mater. Today Commun.*, 2022, **33**, 104683.
26 A. N. Mallika, A. Ramachandra Reddy and K. Venugopal Reddy, *Mater. Res. Express*, 2015, **2**, 095013.
27 J. W. Soares, D. M. Steeves, D. P. Ziegler and B. S. DeCristofano, *Proc. SPIE*, 2006, **6370**, 637011.
28 R. Hong, T. Pan, J. Qian and H. Li, *Chem. Eng. J.*, 2006, **119**, 71–81.
29 C. A. Jaramillo-Páez, J. A. Navío, M. C. Hidalgo and M. Macías, *Catal. Today*, 2018, **306**, 242–249.
30 X. Zhang, Y. Chen, S. Zhang and C. Qiu, *Sep. Purif. Technol.*, 2016, **168**, 178–185.
31 A. Wang, W. Quan, H. Zhang, H. Li and S. Yang, *RSC Adv.*, 2021, **11**, 20465–20478.
32 S. A. Ansari, M. M. Khan, M. O. Ansari, J. Lee and M. H. Cho, *J. Phys. Chem. C*, 2013, **117**, 27023–27031.
33 P. T. Anastas and N. Eghbali, *Chem. Soc. Rev.*, 2010, **39**, 301–312.
34 A. K. Mishra and D. Das, *Mater. Sci. Eng., B*, 2010, **171**, 5–10.
35 S. Kanchana, M. J. Chithra, S. Ernest and K. Pushpanathan, *J. Lumin.*, 2016, **174**, 49–55.
36 S. Kumar, Y. J. Kim, B. H. Koo, S. K. Sharma, J. M. Vargas, M. Knobel, S. Gautam, K. H. Chae, D. K. Kim, Y. K. Kim and C. G. Lee, *J. Appl. Phys.*, 2009, **105**, 07C520.
37 A. Manikandan, E. Manikandan, B. Meenatchi, S. Vadivel, S. K. Jaganathan, R. Ladchumananandasivam, M. Henini, M. Maaza and J. S. Aanand, *J. Alloys Compd.*, 2017, **728**, 1325–1335.
38 A. V. Borhade, D. R. Tope and J. A. Agashe, *J. Mater. Sci.: Mater. Electron.*, 2018, **29**, 6942–6953.
39 F. Li, Y. Yuan, J. Luo, Q. Qin, J. Wu, Z. Li and X. Huang, *Appl. Surf. Sci.*, 2010, **256**, 6076–6082.
40 A. G. Gadhave, V. A. Kadnor, B. U. Patil and B. K. Uphade, *Heterocycl. Lett.*, 2020, **10**, 595–601.
41 G. Xiong, U. Pal, J. G. Serrano, K. B. Ucer and R. T. Williams, *Phys. Status Solidi B*, 2006, **243**, 3570–3575.
42 R. Bomila, S. Srinivasan, S. Gunasekaran and A. Manikandan, *J. Supercond. Nov. Magn.*, 2017, **30**, 3241–3250.
43 K. Raja, P. S. Ramesh and D. Geetha, *Spectrochim. Acta, Part A*, 2014, **129**, 34–40.
44 L. D. S. Yadav, *Infrared (IR) Spectroscopy, Organic Spectroscopy*, Springer, Dordrecht, 2005, pp. 52–106.
45 J. I. Langford and A. J. C. Wilson, *J. Appl. Crystallogr.*, 1978, **11**, 102–113.
46 X. Wei, Q. Li, C. Wu, T. Sun and X. Li, *J. Sci. Food Agric.*, 2020, **100**, 5527–5538.
47 O. Altıntas Yıldırım, H. E. Unalan and C. Durucan, *J. Am. Ceram. Soc.*, 2013, **96**, 766–773.
48 S. Muthukumaran and R. Gopalakrishnan, *Opt. Mater.*, 2012, **34**, 1946–1953.
49 A. Kabalnov, *J. Dispersion Sci. Technol.*, 2001, **22**, 1–12.
50 D. Titus, E. J. J. Samuel and S. M. Roopan, Green Synthesis, Characterization and Applications of Nanoparticles, *MNT*, 2019, **12**, 303–319.
51 H. Wei, Y. Wu, N. Lun and C. Hu, *Mater. Sci. Eng., A*, 2005, **393**, 80–82.
52 M. A. Ismail, K. K. Taha, A. Modwi and L. Khezami, *J. Ovonic Res.*, 2018, **14**, 381–393.
53 R. Bardestani, G. S. Patience and S. Kaliaguine, *Can. J. Chem. Eng.*, 2019, **97**, 2781–2791.
54 M. Zhou, H. Qiao, T. Xia, Z. Wei, L. Zhu and H. Yang, *J. Nanomater.*, 2009, **2009**, 1–5.
55 F. Fang, D. Song, X. Sun, H. Yang, H. Sun, J. Zhu and L. Bai, *Sens.*, 2015, **15**, 20086–20096.
56 A. A. El-Samak, N. O. Eltai, A. Ammar, M. K. Hassan, A. Karim, M. A. A. Al-Maadeed, M. Alser, D. Ponnamma, S. Adham and S. Shurbaji, *ACS Omega*, 2021, **6**, 8081–8093.
57 T. C. Kaspar, S. A. Chambers, P. S. Bagus and T. Droubay, *J. Phys. Chem. C*, 2010, **114**, 21562–21571.
58 X. Bao, T. Schedel-Niedrig, R. Schlögl and M. Muhler, *Phys. Rev. B*, 1996, **54**, 2249–2262.
59 J. Zhang, D. Yu, K. Kakushima, H. Wong and H. Iwai, *AIP Adv.*, 2014, **4**, 117117.
60 Y. Du, Y. Shen, Q. Chen, Z. Yin, M.-S. Zhang and J. Hong, *Appl. Phys. A: Mater. Sci. Process.*, 2003, **76**, 171–176.
61 J. A. Rodriguez and M. Kuhn, *J. Phys. Chem.*, 1996, **100**, 381–389.
62 Y. Inoue and I. Yasumori, *Bull. Chem. Soc. Jpn.*, 1981, **54**, 1505–1510.
63 F. S. Lim, R. T. Ginting, M. Gu, W. S. Chang, Y. Zhu, B. Wu, C. H. Chia, H. Wu, J.-M. Kim, S. T. Tan, K. S. Lau, H. Yu and J.-W. Chen, *J. Phys. Chem. C*, 2020, **124**, 14105–14117.
64 N. Singh, B. K. Allam, D. S. Raghuvanshi and K. N. Singh, *Adv. Synth. Catal.*, 2013, **355**, 1840–1848.
65 A. V. Borhade and B. K. Uphade, *J. Iran. Chem. Soc.*, 2016, **6**, 197–201.
66 D. Shi, J. Mou, Q. Zhuang, L. Niu, N. Wu and X. Wang, *Synth. Commun.*, 2004, **34**, 4557–4563.
67 G. M. Reddy and J. S. Raul Garcia, *J. Heterocycl. Chem.*, 2017, **54**, 89–94.
68 E. Ali, M. Reza Naimi-Jamal and R. Ghahramanzadeh, *J. Chem. Sci.*, 2015, **58**, 235–240.
69 E. Ali, *et al.*, *ChemistrySelect*, 2019, **4**, 9033–9039.

70 B. Maleki, H. Eshghi, M. Barghamadi, N. Nasiri, A. Khojastehnezhad, S. S. Ashrafi and O. Pourshiani, *Res. Chem. Intermed.*, 2016, **42**, 3071–3084.
71 C.-F. Zhou, J.-J. Li and W.-K. Su, *Chin. Chem. Lett.*, 2016, **27**, 1235–1239.
72 G. M. Reddy and J. R. Garcia, *J. Heterocycl. Chem.*, 2015, **52**, 1–5.
73 A. R. Moosavi-Zare, H. Afshar-Hezarkhani and M. M. Rezaei, *Polycyclic Aromat. Compd.*, 2017, **37**, 567–572.
74 H. Kiyani, H. A. Samimi, F. Ghorbani and S. Esmaieli, *Curr. Chem. Lett.*, 2013, **2**, 197–206.
75 D. Azarifar, S.-M. Khatami and R. Nejat-Yami, *J. Chem. Sci.*, 2014, **126**, 95–101.
76 Y. Peng, G. Song and R. Dou, *Green Chem.*, 2006, **8**, 573–575.
77 M. S. Vasava, M. N. Bhoi, S. K. Rathwa, S. S. Shetty, R. D. Patel, D. P. Rajani, S. D. Rajani, A. Patel, H. A. Pandya and H. D. Patel, *J. Mol. Struct.*, 2019, **1181**, 383–402.
78 R. H. Vekariya, K. D. Patel and H. D. Patel, *Res. Chem. Intermed.*, 2015, **41**, 4257–4264.
79 A. Khandebharad, S. Sarda, M. Soni and B. Agrawal, *Bull. Chem. Soc. Ethiop.*, 2019, **33**, 331–340.
80 B. Karmakar, *Aust. J. Chem.*, 2016, **69**, 973–978.
81 L. Khazdooz and A. Zarei, *Iran. J. Catal.*, 2016, **6**, 69.
82 E. Soleimani, M. Jafarzadeh, P. Norouzi, J. Dayou, C. S. Sipaut, R. F. Mansac and P. Saei, *J. Chin. Chem. Soc.*, 2015, **62**, 1155–1162.
83 H. Mecadon, M. R. Rohman, M. Rajbangshi and B. Myrboh, *Tetrahedron Lett.*, 2011, **52**, 2523–2525.
84 S. U. Tekale, *et al.*, *J. Chem.*, 2013, **2013**, 840954.
85 S. Ambethkar, V. Padmini and N. Bhuvanesh, *J. Adv. Res.*, 2015, **6**, 975–985.